Proceedings of 2001 Korea-Japan Joint Seminar
on Particle Image Velocimetry
Seoul National Univ., Dec. 3 - 4

Industrial Applications of PIV/PTV Velocity Field Measurement Techniques

Sang Joon Lee

Department of Mechanical Engineering
Pohang University of Science & Technology (POSTECH)
San 31, Hyoja-dong, Nam-gu, Pohang, 790-784, Korea.

ABSTRACT Due to advances in digital image processing, computer and optical hardware, it is possible to extract full flow information from visualized flow images. Recently, the PIV/PTV methods have been accepted as a reliable velocity field measurement technique. In my laboratory, several velocity field measurement techniques have been developed and they were applied to various thermo-fluid flow problems. In this paper, some of the industrial applications will be discussed. As a result, the PIV/PTV technique was proved to be a powerful tool for industrial fluid flow diagnosis.

1. Velocity Field Measurement Techniques

The velocity field measurement technique, commonly named PIV, provides instantaneous velocity fields over the entire image frame. If the image frames are consecutively recorded, we can investigate the evolution of time varying flow fields. By averaging the instantaneous velocity field data, we can acquire spatial distribution of turbulence statistics such as turbulence intensity, Reynolds shear stress, turbulent kinetic energy, etc. The PIV technique also can be applied to complex turbulent flows such as separated shear flows or chemically reacting flows. In my laboratory, several PIV/PTV velocity field measurement techniques such as the 2-frame PTV, hybrid adaptive PTV, recursive 2-frame PIV, single-frame PIV, and 3-D stereoscopic PIV methods have been developed and applied to various thermo-fluid flows.

The 2-frame PTV technique based on match probability has been applied to various turbulent flows: backward-facing flow, flow around a vertical fence, wake behind a porous fence, ship wake, flow around an axial fan, turbulent boundary layer over semi-circular riblets, etc. From these experiments, it was found that the ensemble averaging of at least 400 instantaneous velocity fields is needed to obtain reliable spatial distribution of turbulence statistics, however, about 100 velocity fields are sufficient for the mean velocity field.

The adaptive hybrid PTV method combined the merits of both of the 2-frame PTV and conventional cross-correlation PIV methods. It has been applied to turbulent flow around a 2-D vertical solid fence, porous fence with bottom gap, micro-channel flow, flow around NACA0012 with flexible micro-riblet, etc. As industrial applications, the hybrid PTV was employed to measure the flow inside accumulator of rotary compressor and flow around a ship propeller.

The recursive 2-frame cross-correlation PIV method developed recently was applied to several complex flows; ventilation flow in a vehicle passenger compartment, ventilation flow in a large factory building, wake behind a cylinder with micro-riblet, wake behind a container ship model, and high-speed suction flow into a vacuum cleaner.

The single-frame double-exposure PIV technique using a 2K × 2K high-resolution CCD camera has been applied to the turbulent flows of elliptic jet, buoyant jet, wake behind elliptic cylinders close to free surface, oil fence flow and flow around a ship model. As industrial applications, it was applied to the flow inside snout and to the molten Zinc flow of the continuous hot-dip galvanizing process.

2. Wind Erosion Problem of Open Storage Coal Yard (POSCO)

2.1 Introduction

The wind erosion of small particles such as snow and sand in the region of strong wind has been one of the important wind engineering problems over the past several decades. The wind-erosion phenomena occur frequently at open storage yards of a power generation plant or steel company, and it causes environmental problems in addition to the loss of raw material itself. At POSCO located at the south-eastern seaside of Korea peninsula, coal dusts of open storage yard are blown by strong wind and local gusts, especially in the summer stormy season. In order to abate wind erosion of coal dusts, we proposed to install a porous wind fence around the coal yard.

Despite its practical importance, the flow around coal piles behind a porous wind fence has received relatively little attention due to its complex flow structure. It has been known that the wind erosion phenomena were closely related to the flow characteristics near the surface, especially the mean velocity and the wall shear stress. Borges & Viegas (1988) studied the shelter effect of porous fences on the coal pile by measuring the velocity defect and the shear stress distribution. They found that the surface shear stress decreased as the ratio of the fence height to the crest height of the coal pile increased.

2.2 Flow structure of porous fence wake (2-frame PIV)

The experiment was carried out in a circulating water channel of which the test section size was $300^{W}\times200^{H}\times1200^{L}$(mm). A schematic diagram of the fence and prism model with coordinate system used in this study is shown in Fig.1. The fence model was made of stainless steel of 0.3mm thickness (B). The fence height (H) was 25mm and had a flat end. Since the shape ratio (B/H=0.012) is less than 0.33, the flow can be regarded as a fence flow. The porous fence had a geometric porosity (open area percentage) ε=38.5% consisting of uniformly distributed circular holes. From preliminary study, this fence porosity was found to be good for velocity and turbulent momentum reduction.

A triangular prism was located at X=1H behind the wind fence. The crest height (h) of the prism was 17mm. During the experiments, the free stream velocity was maintained at 12.5cm/s and its corresponding Reynolds number (Re) based on the fence height was about 3,460. Local Reynolds number (Re_x) based on the fence location was 1.11×10^5. A tripping wire was installed at inlet of the test section to make the fence and prism to be fully submerged in a turbulent boundary layer.

The 2-frame PTV system consisted of a laser light sheet, CCD camera, frame grabber and computer. A 4W Ar-ion laser provides a thin laser light sheet of approximately 3mm in thickness by passing through a fiber-optical cable and cylindrical lens. Polystyrene particles with a mean diameter of 150μm were seeded before the experiment. Velocity field measurements were made at three consecutive cross-sections along the central plane of the water channel. For more detail of the two-frame PTV algorithm and its accuracy, see the reference [2]. In this experiment, a total of 350 instantaneous velocity fields were acquired at each measurement section. Mean velocity field was obtained by ensemble averaging of the 350 instantaneous velocity vector fields on the grid points (43×42 grids).

The mean velocity vector fields around a triangular prism model with and without a porous fence installed are shown in Fig.2. Without the wind fence, the oncoming flow is accelerated along the windward side of the prism and separated near the prism crest. When a wind fence with porosity ε=38.5% is installed in front of the prism, from the shelter effect of the fence the mean velocity is largely reduced between the fence and prism model. In addition, the approaching flow is separated at the top edge of the fence and the upper part of prism model is located below the separated shear layer developed from the fence.

Comparison of the turbulent kinetic energy profiles for the cases with and without the wind fence is shown in Fig.3. The general shape is similar to the streamwise turbulence intensity. This results from the fact that the vertical turbulent intensity is about half of the streamwise turbulent. Due to the existence of fence, the turbulent kinetic energy has higher values above the fence height. On the other hand, it has much smaller values in the wake region below the fence height. Especially, at the prism crest, the porous wind fence reduces the turbulent kinetic energy down to 1/3 of that without the fence.

2.3 Effect of bottom gap (Hybrid PTV)

Fig.4 shows the instantaneous velocity vector fields around the porous fence having porosity of ε=38.5% for various gap ratios (*G/H*). The oncoming flow is divided into two directions in front of the fence; one moves upward and passes over the fence top and the other goes downward and passes the bottom gap between the lower edge of the fence and the bottom plate. There is no distinct re-circulation flow behind the porous fences irrespective of the gap ratio. The reduction of velocity by the porous fence is dominant and clear in the near wake behind the fence. As the bottom gap increases, the gap flow passing through the bottom gap becomes strong. As the flow goes downstream, the region affected by the gap flow is gradually expanded.

The shelter parameter proposed by Gandemer(1979) reflected only the streamwise mean velocity and turbulence intensity. Though the vertical velocity component is relatively small, compared with the streamwise velocity component, it has to be considered in addition to the streamwise velocity component to get accurate shelter parameter. Therefore, a modified shelter parameter ψ that takes into account both the streamwise and vertical velocity components was proposed as follows;

$$\psi = \left(|U| + \sqrt{\overline{u'^2}} + |V| + \sqrt{\overline{v'^2}} \right) / \left(U_o + \sqrt{\overline{u_o'^2}} \right)$$

Fig.5 shows contour plots of the shelter parameter as a function of the gap ratio. The shelter parameter ψ in the upper shear layer shows similar contours, irrespective of the gap ratio. The region having significant values is expanded as the flow goes downstream. In the lower shear layer, the shelter parameter ψ increases and the region having large ψ values is expanded as the gap ratio increases. The shelter parameter in the bleed flow region just behind the fence has small values. For the gap ratio of *G/H=0.3*, the large gap flow through the bottom gap space makes the region having small ψ values move upward. The porous fence with the gap ratio *G/H=0.1* gives a good shelter effect similar to the no gap fence.

2.4 Field test

Reflecting the previous test results including threshold velocity measurement of wind-blown sand particles stacked behind the wind fence, the porous wind fence of porosity ε=30% was installed in part (east and north sides) around Yard 5 of Kwang-Yang open storage yard with US $4,000,000 investment. Fig. 6(a) shows the photograph of the porous wind fence installed around Yard 5. The fence height is 17m and total length is about 1,800m.

Fig. 6(b) shows the monthly wind-blown dust concentration measured around the open storage yard. The wind-blown dust concentrations were measured twice in a month at two measurement points. The wind-blown dust concentration is defined as the total mass of suspending particles per unit volume (TSP, $\mu g/m^3$). It was about 1,300$\mu g/m^3$ before the installation of wind fence, beyond the environmental regulation limit of 1,000 $\mu g/m^3$. However, the environmental regulation limit of the wind-blown dust was enhanced as to 500 $\mu g/m^3$ from the end of 1998. The vertical axis is non-dimensionalized by a corresponding regulation limit value. By installing the porous wind fence, the wind-blown dust concentration is largely reduced below the environmental regulation limit. The TSP concentration is reduced up to 70-80% compared with that for the no fence case. This implies that the porous wind fence installed along two sides of the Kwang-Yang open storage yard is very effective for abating wind-blown coal dusts.

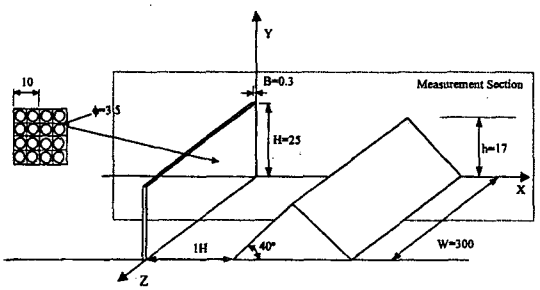

Fig.1 Schematic diagram of fence and prism model with a coordinate system (unit:mm)

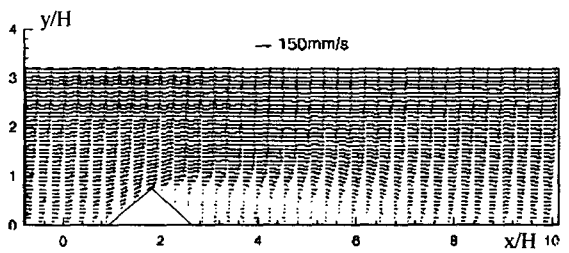

(a) Without fence

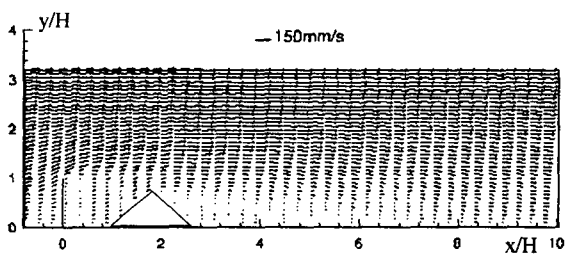

(b) With fence

Fig.2 Comparison of mean velocity vector fields with and without the wind fence

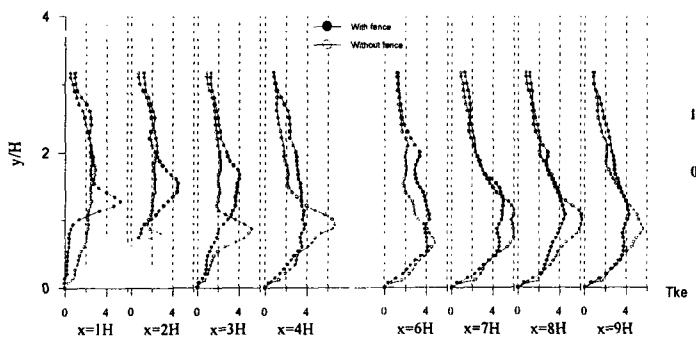

Fig.3 Comparison of turbulent kinetic energy profiles with and without the wind fence

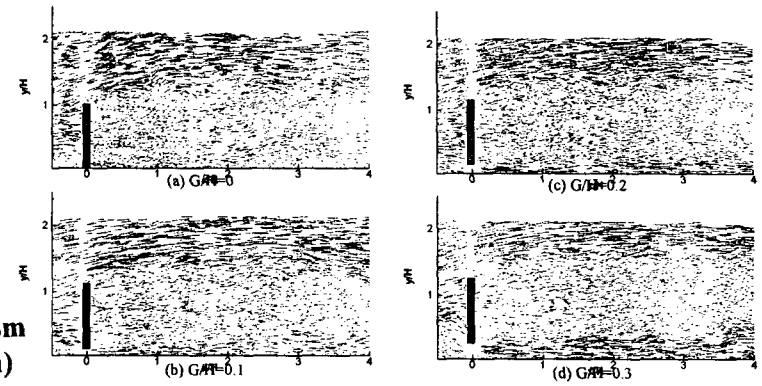

Fig.4 Effect of bottom gap on instantaneous velocity fields for a porous fence

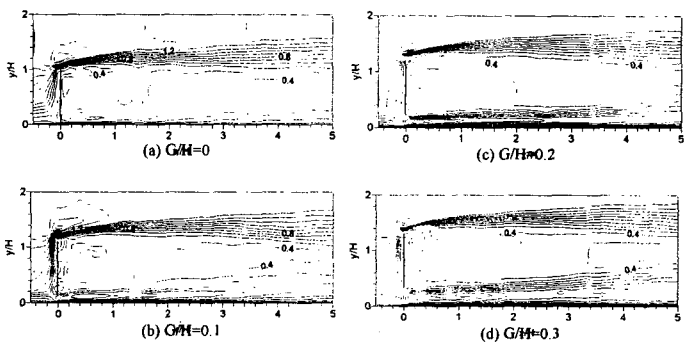

Fig.5 Contour plot of shelter parameter as a function of the gap ratio

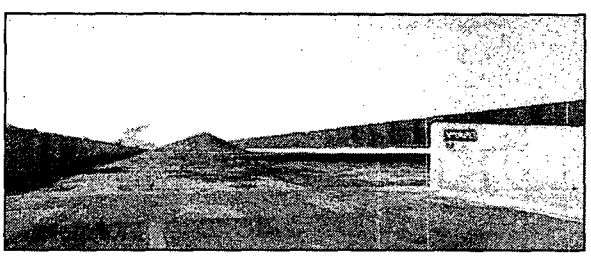

(a) Wind Fence Installed at Kwang-Yang Works

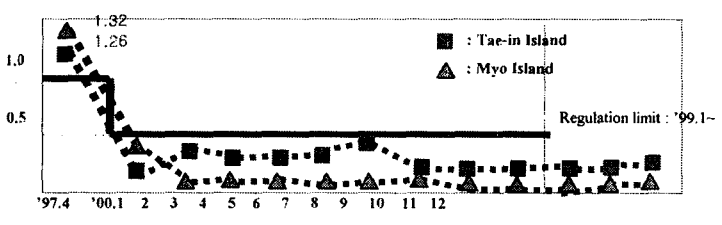

(b) Dust Reduction

Fig.6 Wind fence installed at Kwang-Yang work and wind-blown dust reduction

3. Improvement of Ventilation Flow in a Factory Building (HHI)

3.1 Introduction and experimental apparatus (2-frame PIV)

In a huge shipbuilding factory building, typical harmful factors giving unpleasant feeling include fume or vaporized gas resulted from a welding & cutting process, dusts from grinding and all sorts of noise. One of the best ways to reduce these harmful factors is to increase the efficiency of natural ventilation. The atmospheric wind around the building, the location and size of vents, ventilation devices, and the arrangement of internal structures inside the building affect largely the indoor ventilation inside the building. Therefore, it is important to have a complete understanding on ventilation flow to provide a safe and comfortable working environment. In order to utilize the natural ventilation effectively, the study on the modification of opening vents in a shipbuilding factory building was carried out. Instantaneous velocity fields inside the 1/1000 scale-downed factory model were measured using a 2-frame PIV system.

Instantaneous velocity fields inside the factory model were measured using a 2-frame PIV system. The velocity field measurement system consists of a two-head Nd:Yag laser, a high-speed CCD camera, a synchronizer and an IBM PC as shown in Fig.7. The two-head Nd:YAG laser has 7ns pulse duration and 25mJ light intensity per pulse. The flow images were captured using a high-speed CCD camera (Speedcam$^+$ 512) which can capture images at a sampling rate of 1000fps(frame per second) with a full resolution of 512×512 pixels. Vaporized olive oil particles of average diameter of 2μm were seeded as tracer particles.

The horizontal plane at y=6.5mm height from the ground was divided into 31 sub-sections as shown in Fig.8. For each sub-section of about 60×60mm^2, instantaneous velocity fields were measured for three wind directions - northwest, northeast and southeast. These wind directions were found to be dominant yearly around the building in field test. Bold lines in Fig.8 show the locations of the opening vents in a factory model.

3.2 Local ventilation flow

Fig.9 shows the instantaneous velocity field at the central subsection No. 14 for north-east wind. The flow field inside the modified model(I) doesn't show any differences from the current ventilation model(Fig.9(a)). From this point of view, we can see that the openings of the modified model(I) are not effective for the north-east wind. They do not contribute to exhausting the contaminants generated in the central region. The modified model(II) has opening vents in the center of the east-side wall and they are facing the northeastern wind directly. As shown in Fig.9(c), the modified model(II) improves ventilation flow in the central section of the model and increases the overall airflow rate. From the results for three wind directions, we found that the opening vents and

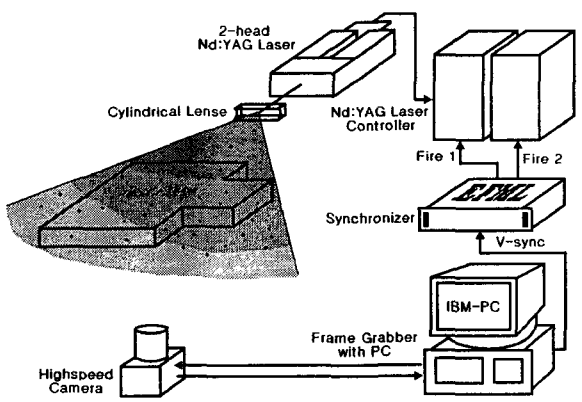

Fig.7 PIV system for measuring velocity field of ventilation flow inside a factory building.

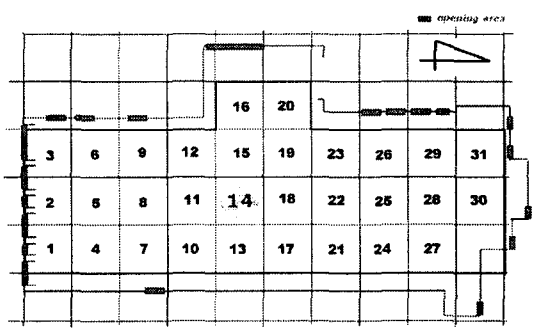

Fig.8 Velocity field measurement sections with opening locations.

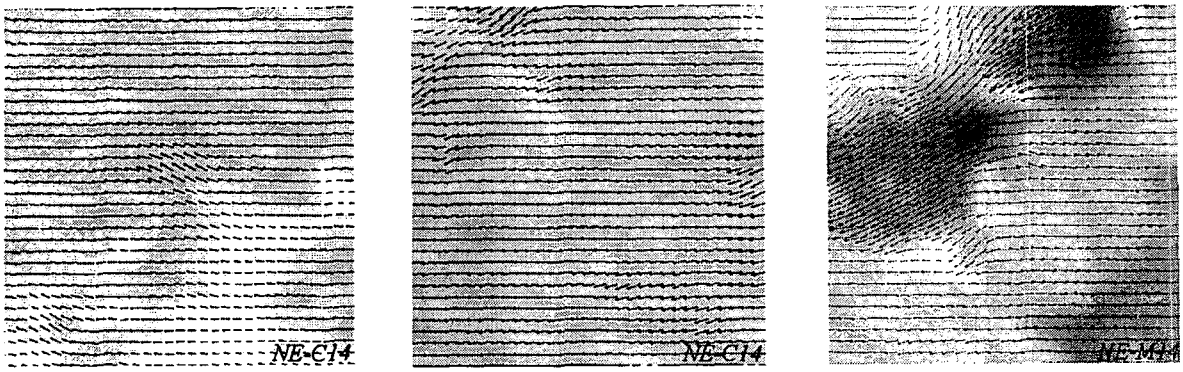

(a) Existing model (b) Modified model(Ⅰ) (c) Modified model(Ⅱ)

Fig.9 Comparison of velocity fields at section 14 for north-east wind

galleries in the east and north walls have to be modified to increase the overall airflow inside the building.

3.3 Overall ventilation flow

The instantaneous velocity fields in the whole building for the north-east wind are compared in Fig.10. Some local instantaneous velocity fields are partly mismatched in the velocity filed due to combination of total 31 subsections into one. However, they show clearly overall ventilation flow characteristics inside the model.

For the current model, the ventilation flow inside the building is slow and nearly stagnant. The modified models(Ⅰ), (Ⅱ) show different dependence on wind direction. For example, the effect of the ventilation improvement on the north-east wind is not good for the modified model(Ⅰ), even though it has more vents than the modified model(Ⅱ).

Fig. 10(c) shows that the modified model(Ⅱ) improves the internal ventilation flow with increasing the flow speed more than two times, compared with that of present ventilation system. From a practical point of view, the modified model(Ⅱ) seems to be most effective and economic modification for improving the ventilation problem inside the factory building.

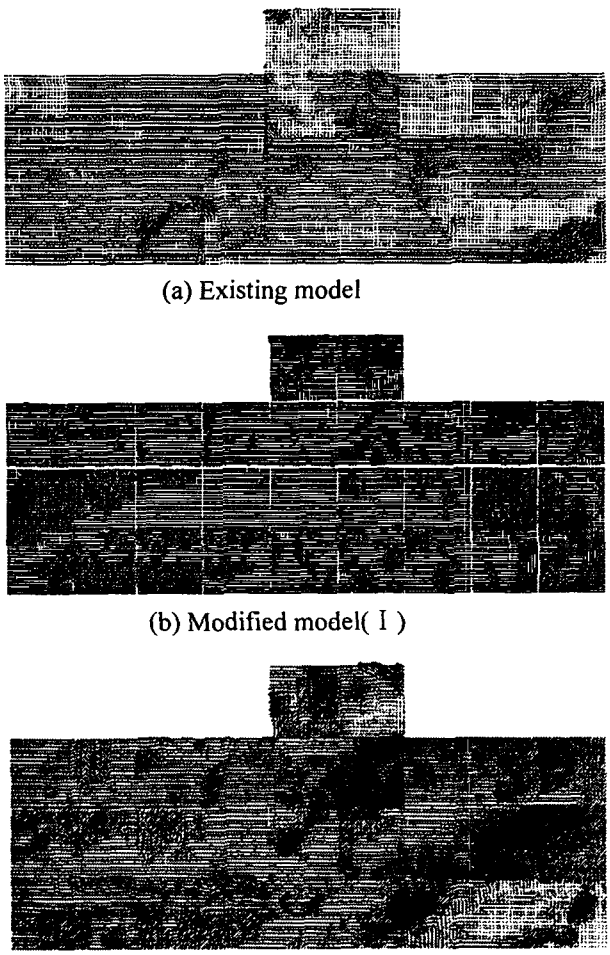

(a) Existing model

(b) Modified model(Ⅰ)

(c) Modified model(Ⅱ)

Fig.10 Velocity fields within the building for north-east wind.

4. Flow Analysis of a Molten Zinc Pot (POSCO)

4.1 Introduction and experimental apparatus (Single-frame PIV)

Many heavy industries such as automobile and home appliance industries demand high quality zinc-plated steel strips. However, in continuous hot-chip galvanizing process, drosses are formed due to metallic compounds and chemical reaction when a long steel strip continuously passes through the molten Zn pot. These drosses attach to the strip surface, degrading the quality of zinc-plated steel sheets. In order to resolve this problem, several studies on the flow inside the molten pot were carried out. However, most of previous studies on zinc plating process were qualitative analyses such as flow visualization with a simple water model. Some have focused on flow around the sink roll.

In this study, a transparent water model of the zinc-plating process including the snout, a pair of induction heaters and scrappers was made to investigate the flow inside the Zn pot. With varying several parameters including the flow rate of the induction heaters, scraper location and baffle configuration, the instantaneous velocity fields of flow inside the Zn pot were measured using the single-frame double-exposure PIV system.

Fig. 11 shows the schematic diagram of water model consisting of a rotating sink roll, an endless moving strip made of rubber band, a pair of induction heaters, stabilizing rolls, a snout and scrappers. It is a 1/5 scale-down model of a zinc plating plant of POSCO KwangYang works and the bottom surface of Zn pot was curved to maintain geometric similarity.

The endless moving strip was rotated by a DC motor and its speed was controlled by adjusting voltage output of the DC power supply. Two induction heaters were installed near the snout on side of the Zn pot. Each induction heater was driven by a pump located outside and the working fluid in Zn pot was re-circulated. PIV velocity field measurements were carried out on the central plane. The working fluid used in this study was distilled water.

The PIV system was consisted of a high-resolution CCD camera, a 2-head Nd:YAG laser, an image grabber, a synchronizing device and a computer as shown in Fig. 12. A high-resolution CCD camera (SMD 4M4) with a resolution of 2k×2k pixels was used to capture particle images. The CCD camera and the Nd:YAG laser were synchronized using a home-made control circuit.

The conventional single-frame PIV method encounters inherently the directional ambiguity problem in determining velocity vectors. The CCD camera used in this study has a special built-in image-shifting feature that is ideal for resolving the directional ambiguity. During the time interval Δt=1ms between two laser pulses, the whole pixel lines of the CCD sensor array are translated a few lines (9 pixels in this study). Therefore, the second particle image shifted exact distance corresponding the translated pixel lines is superimposed on a single-frame of the CCD camera.

Vestosint 1111 particles of 100mm in diameter were used as seeding particles for the liquid flow in the Zn pot. The central plane of the flow inside the Zn pot was illuminated with a pulsed laser light sheet. The high-resolution CCD camera was installed perpendicular to the laser light sheet to capture the scattered particle image of the flow field. The double-exposure single-frame image is then cross-

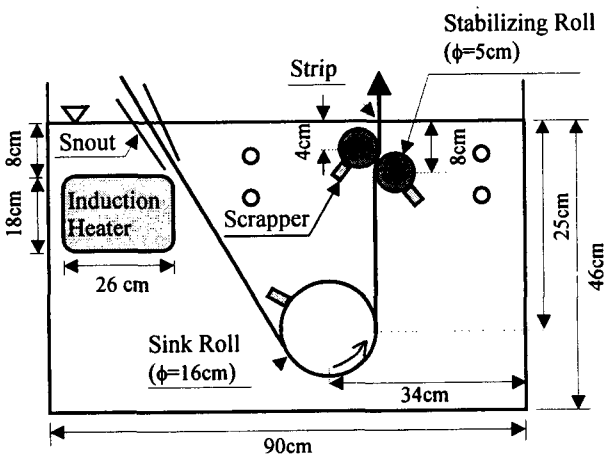

Fig.11 Schematic diagram of 1/5 scale water model.

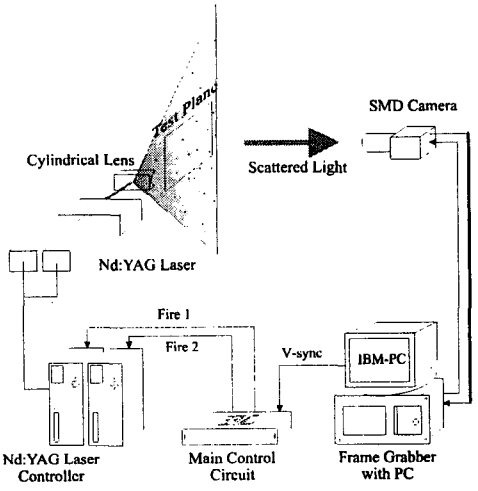

Fig.12 Schematic diagram of the single-frame double-exposure PIV system.

(a) Q=0 lpm (b) Q=28 lpm

Fig.13 Velocity fields around the stabilizing rolls for different flow rate Q of induction heater

correlated to extract velocity vector field. In this study, the interrogation window size was 64×64 pixels and overlapped in 50%.

4.2 Velocity field

In this study, we focused on the flow around the stabilizing roll located in the exit region to solve the top dross problem. PIV measurements were carried out at two sections, both sides of the moving strip. The field of view was 15×15 cm^2 and the moving speed of the strip was fixed at V_S=2.0 m/s.

Fig. 13 shows instantaneous velocity fields around the stabilizing roll in terms of the flow rate of the induction heater. When the induction heater is not operated, the ascending flow is blocked by the stabilizing roll and separated from the strip. The separated flow is guided along the scrapper attached on the stabilizing roll, thereafter it was divided into two parts in the outside region. One ascends toward the upper region of the molten pot and forms a weak counter-clockwise rotating flow. In the lower region between the strop and scrapper, high-speed vortices are formed. In the inner region of the strip, a pair of vortices is formed.

On the other hand, when the induction heater is operated, the ascending flow in the outside region of the molten pot becomes weaken due to the operation of the induction heater. The speed of counter-clockwise rotating flow around the stabilizing roll in the outside region is decreased. However, the flow below the stabilizing roll in the inner and outer parts of the strip becomes strong due to addition of momentum from the induction heater.

Fig. 14 shows the effect of baffle on the flow field around the stabilizing roll. Two baffle were tested at V_S=2.0 m/s and Q=40 lpm. The B type baffle installed in the inner region of the strip is about 3 times larger than the A type baffle. The result shows that both baffles reduce the flow entrainment into the corner region between the strip and stabilizing roll. Comparing the flow fields of two cases, the B type baffle seems to give a better (tranquil) flow around the stabilizing roll. But, in this case, counter-clockwise vortices are formed below the baffle installed in the inner region of the strip.

From these results, we can see that the flow around the stabilizing roll becomes tranquil with attaching a scrapper is attached on the stabilizing roll and adding a baffle near the moving strip. This kind of flow control method will be helpful for reducing the top-dross attachment on steel strips.

(a) A type baffle (b) B type baffle

Fig. 14. Velocity fields around the stabilizing rolls for different baffle type (Q = 40 lpm)

5. Flow inside accumulator of a rotary compressor (LG Electronics)

5.1 Introduction and Experimental Apparatus (Hybrid PTV)

Rotary compressor has been used in many home applications such as refrigerator and air conditioner. Since most of those home appliances are located inside a room, the compressor requires not only a high degree of efficiency but also the silence when it operates. Therefore, the compressor should be designed to satisfy to two goals - high efficiency and low noise.

The accumulator in rotary compressor is an important component from standpoints of compressor cost, performance, sound and ability of controlling excess liquid refrigerants. The primary function of accumulator in a rotary compressor is to separate and collect liquid-phase refrigerants from suction stream of mixture of refrigerant and lubricant oil. If the liquid refrigerant is allowed to rush into the compressor body, mechanical damage may occur. All accumulators are equipped with filtering screen to remove debris. In the sense of sound, while the accumulator acts as an acoustic muffler in one hand, it also acts as a noise generator. Therefore, a compromise between the noise and performance is needed in the design process of accumulator.

It is generally known that the flow inside the accumulator is pulsating with about 60Hz and the pressure at the inlet part is about 5 ~ 6 kgf/cm^2. Therefore, it is very important to understand the flow structure inside the accumulator in detail to enhance the performance and reduce acoustic noise. Due to complex geometric shape and high-pressure pulsating flow characteristics, however, it was nearly impossible to measure the flow inside the accumulator using the conventional velocity measurement instruments.

In this study, the pulsating flow fields inside the proto-type accumulator in the real working condition were investigated experimentally using the hybrid PTV system.

Fig.15 shows the experimental set-up of this experiment. The accumulator model and rotary compressor are attached as a part of the room air-conditioner. The accumulator attached at the inlet of rotary compressor consists of inlet part, screen holder, tube holder, and standpipe as shown in Fig. 16. The mixture of refrigerant and lubricant oil comes in through the upper inlet part of accumulator. The shape of screen holder is very important for separation of liquid coolants. The tube holder supports the standpipe through which the gas phase refrigerants moves into the compressor chamber of compressor main body. The sidewall was made of tempered transparent glass to resist the high-pressure pulsating flow inside the accumulator. In order to avoid the distortion of particle images due to the curved surface of accumulator, four sides of accumulator were covered with same tempered glass. The screen and tube holders have 6 holes with 60° intervals as shown in Fig.15. The hybrid PTV system used for measuring velocity field consists of a two-head Nd:YAG laser, a high-resolution CCD camera (2Kx2K pixel^2), delay generator, pressure sensor, accelerometer and a IBM PC.

In the real working condition, the flow inside the accumulator undergoes periodical pulsating motion, since the rotary compressor rotates at about 3400rpm. Therefore, the hybrid PIV system was synchronized with the phase of the period cycle of internal flow. For this, we installed a pressure transducer and an accelerometer sensor as shown in Fig.16. The pressure sensor (Kistler 6001) was installed at the outlet of accumulator to measure the dynamic pressure. The signal from the pressure sensor undergoes low-pass filtering and amplification using charge amplifier. The amplified signals were used as the input signal of delay generator.

Fig.17 shows typical pressure signal obtained during the experiments. The pressure signal shows that the compressor rotates about 3400rpm and one period is about 17.7msec. The pressure signal has its local maximum and minimum in one period. We determined the location of maximum voltage of pressure signal as a start point and one cycle was divided into 4 phases with 4msec delay time interval from the starting maximum point.

The hybrid PTV measurements were performed at two sections. The upper section includes the screen holder in the middle. The size of each measurement section is about 6cm x 6cm. At section 1, the flow speed is high so the time interval between two particle images was set to $\Delta t = 50\mu$sec. For the section 2, however, the time interval was set to $\Delta t = 550\mu$sec. One hundred particle images were captured in each section and fifty instantaneous velocity vector fields were obtained. By ensemble

averaging these instantaneous velocity fields, the phase-averaged velocity vector fields were obtained at 4 different phases.

During experiments, the inlet pressure of accumulator was maintained at 5.5 kgf/cm^2 and the outlet pressure of compressor was fixed 18 kgf/cm^2 to match the real operating condition. In addition, the room temperature was maintained at 26°C.

5.2 Velocity field measurements

Fig.18 shows the phase-averaged mean velocity fields and speed contours measured at section 1 above the tube holder. The impinged flow structure is shown in the central region above the screen holder and large-scale vortex structure is formed in the corner between the inner wall of accumulator and the screen holder surface.

The change of global mean velocity field with respect to the compressor phase is not so large at section 1 above the screen holder. However, in the region between the screen holder and tube holder, the flow structure is changed clearly according to the phase. In phase 1, the flow passed the hole of screen holder moves vertically downward direction, Most of them move downward along the stand tube wall and a little goes into the stand tube. The flow structure below the screen holder was changed periodically with varying the phase. The bleed flow passing the screen holder starts to curve toward the inlet of stand tube at phase 2. As the phase angle increases, the flow more curved toward the standtube. At phase angles 3 and 4, most of the bleed flow goes directly to the tube inlet.

The flow near the tube holder also varies according to the phase angle. At phase 1, some flow separates the holes of tube holder and moving downward at low speed. With approaching to phase 2, the flow above the tube holder becomes tranquil and a large-scale vortex is formed between the sidewall and tube holder, although its strength is weak. As the phase angle increases from phase 2 to phase 3, the speed of upward flow penetrating the holes of tube holder increases. The negative outlet pressure at phases 2 and 3 makes the flow below the tube holder moves upward from the lower part of accumulator. The downward flow passing through the holes of screen holder is pushed by this upward flow and bent toward the inlet of standtube. That is, as the negative pressure at the outlet of accumulator increases, the suction power inside the standpipe is enhanced. This makes the upward flow passing through the tube holder grows and causes the bleed flow passing the screen holder to move directly into the standtube.

Since the main function of accumulator is to separate the liquid refrigerant, the direct entering of mixture of refrigerant and oil into the standtube may increase the possibility of entering liquid refrigerant. This possibility should be reduced in order to increase the accumulator performance.

As a conclusion, the velocity fields of flow inside the accumulator of a rotary compressor working at the real condition were measured quantitatively using the phase-averaging PTV velocity field measurement technique and confirmed the periodic pulsating flow characteristics according to compressor phase.

6. Conclusion

The PIV/PTV velocity measurement techniques developed in our laboratory have been applied to various industrial thermo-fluid flows. Most of these industrial problems could not be solved with simple qualitative flow visualization techniques or conventional point-wise velocity measurement instruments such as Pitot tube, hot-wire, and LDV. In order to resolve the industrial thermo-fluid problems successfully, the PIV/PTV velocity field measurement system should have larger dynamic velocity range, higher spatial and temporal resolution, large field of view, higher measurement accuracy with small error vectors, etc. Most of all industrial applications carried out was successful and some of the results were adopted on the spots or our proposal was applied on the field process directly. As a conclusion, the PIV/PTV methods were very effective and most economic in the viewpoints of time and endeavors required to solve the given problems. The PIV/PTV technique was proved to be a powerful tool for industrial fluid flow diagnosis.

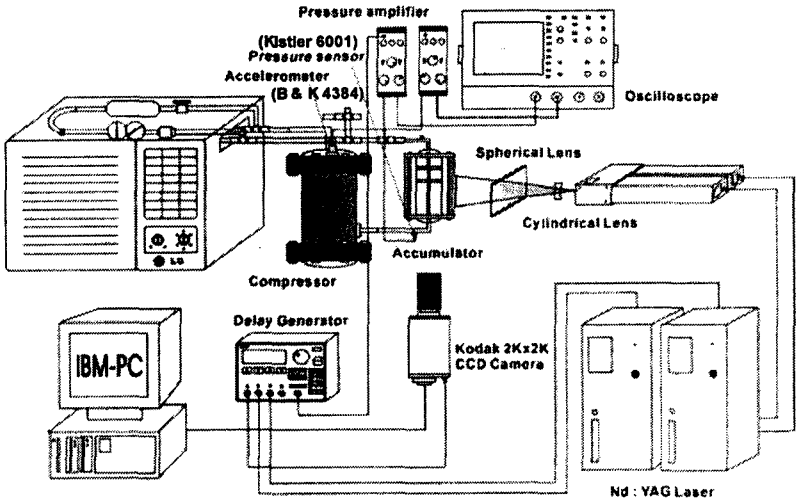

Fig.15 Schematic diagram of experimental set-up

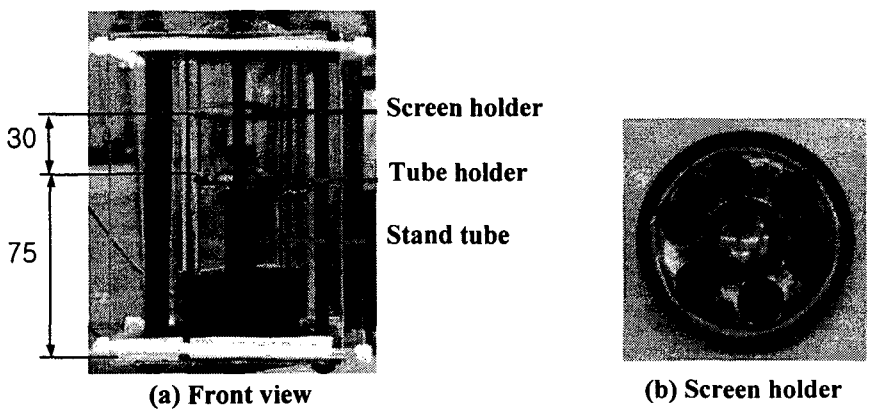

(a) Front view

(b) Screen holder

Fig.16 Configuration of accumulator model (unit: mm)

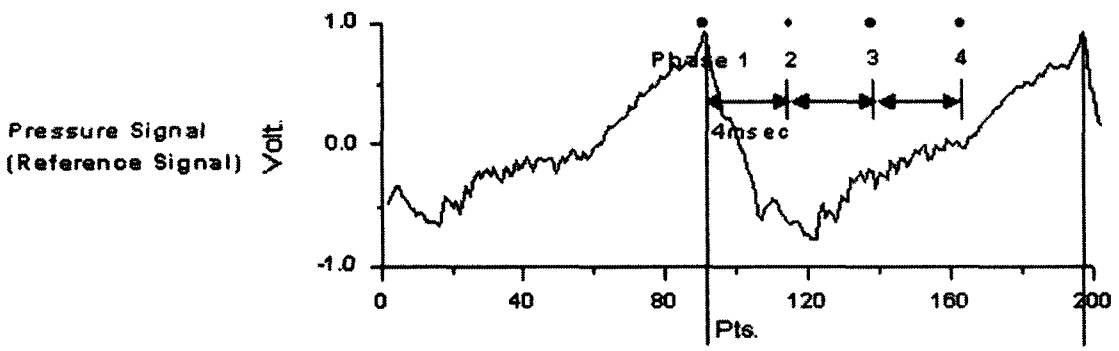

Fig.17 Typical voltage signals of the pressure transducer

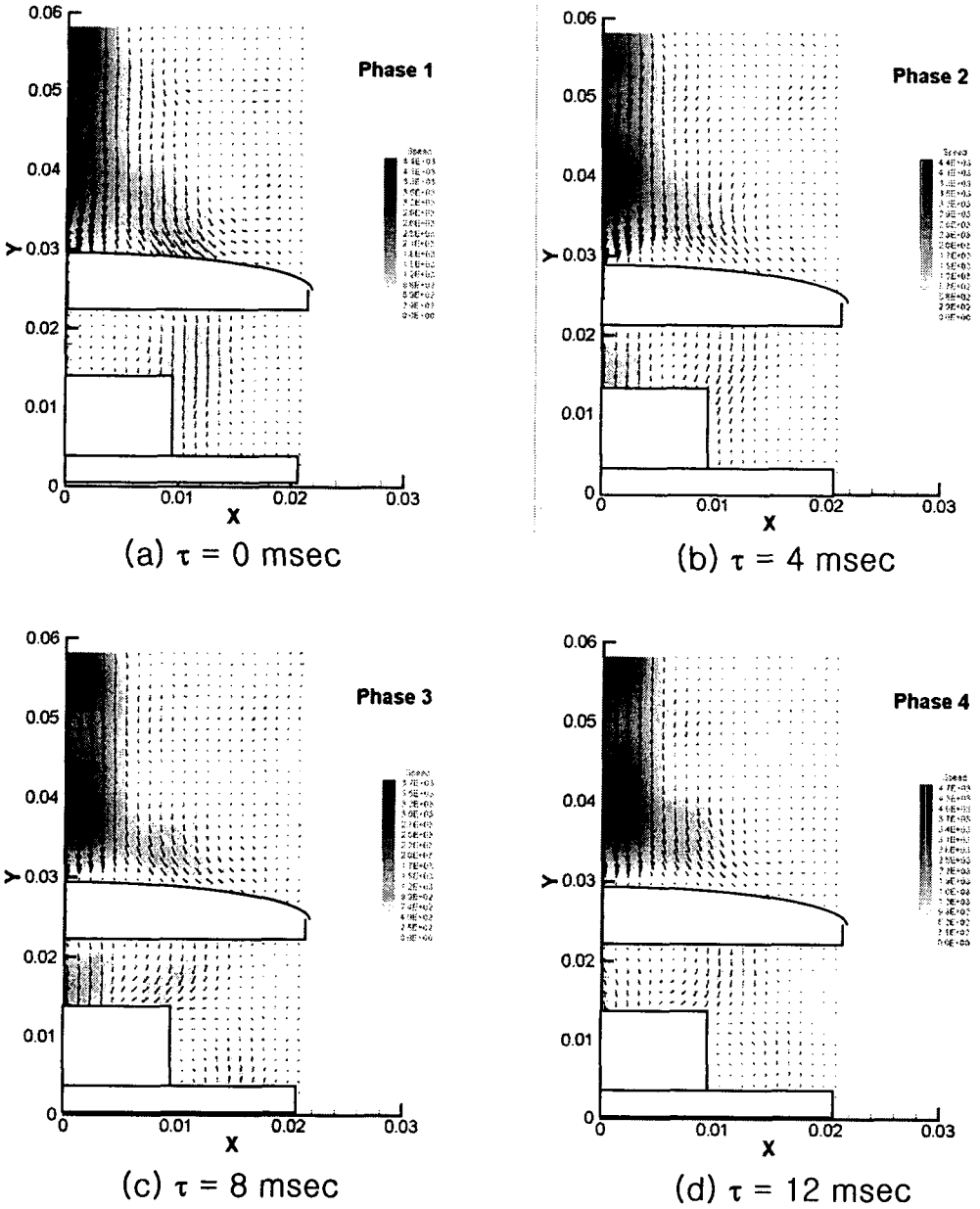

Fig.18 Phase-averaged velocity field variations with respect to phase angle

Acknowledgement

This study was sponsored by NRL(National Research Laboratory) program of the Ministry of Science and Technology, Korea

References

1. R.J. Adrian, 1991, "Particle imaging techniques for experimental fluid mechanics", Annual Rev. of Fluid Mech., Vol.23, pp.261-304
2. S.J. Baek and S.J. Lee, 1996, "A new two-frame particle tracking algorithm using match probability", Experiments in Fluids, Vol.22, pp.23-32
3. S.J. Baek and S.J. Lee, 1996, "Velocity field measurement of wake flow behind a ship model", Proc. 3rd Korea-Japan Joint Workshop on Ship & Marine Hydrody., Daejon, Korea, pp.57-64
4. A.R. Borges and D.X. Viegas, 1988, Shelter effect on a row of coal piles to prevent wind erosion, J. Wind Eng. Industrial Aerodyn., Vol.29, pp.145-154
5. E.A. Cowen and S.G. Monismith, 1997, "A hybrid digital particle tracking velocimetry technique", Experiments in Fluids, Vol. 22, pp.199-211
6. DaiChin and S.J. Lee, 2001, "Flow structure of the wake behind an elliptic cylinder close to a free surface", KSME Int. J, Vol.15(12), pp.1207-1216,
7. J. Gandemer, 1979, "Wind shelters", J. Industrial Aerodyn., Vol. 4, pp.371-389
8. H.B. Kim and S.J. Lee, 2001, "Hole Diameter Effect on Flow Characteristics of Wake behind Porous Fences Having the Same Porosity", Fluid Dynamic Research, Vol.28(6), pp.449-464
9. H.B. Kim and S.J. Lee, 2001, "Time-resolved velocity field measurements of separated flow in front of a vertical fence", Experiments in Fluids, Vol.31, pp.249-257
10. H.B. Kim and S.J. Lee, 2001, "The structure of turbulent shear flow around a two-dimensional porous fence with a bottom gap", J. of Fluids & Structures, Vol.16(3), in press
11. H.B. Kim and S.J. Lee, 2001, "Performance Improvement of a two-frame PTV using a hybrid adaptive scheme," Meas. Sci. & Tech., accepted
12. R.D. Keane, R.J. Adrian and Y. Zhang, 1995, "Supper-resolution particle image velocimetry," Meas. Science & Technol., Vol.6, pp.754~768
13. S.J. Lee, J.H. Choi and I.S. Lee, 2001, "Velocity field measurements of swirl flow around a forward-swept axial-fan using a phase-averaged PTV technique", J. of Visual, Vol.4, pp.257-265
14. S J. Lee and H.B. Kim, 1999, "Laboratory measurements of velocity and turbulence field behind porous fences", J. Wind Eng. & Industrial Aero., Vol.80, pp.311-326
15. S.J. Lee and H.B. Kim, 1998, "Velocity field measurements of flow around a triangular prism behind a porous fence", J. Wind Eng. & Industrial Aero., Vol.77, pp.521-530
16. S.J. Lee and S.H. Lee, 1999, "Synchronized smoke-wire technique for flow visualization of turbulent flows", Journal of Flow Visualization & Image Processing, Vol. 6, pp.65-78
17. S.J. Lee and S.H. Lee, 2000, "Flow field analysis of turbulent boundary layer over a riblet surface", Experiments in Fluids, Vol.30, pp.153-166
18. S.J. Lee and C.W. Park, 1998, "Surface-pressure variations on a triangular prism by porous fences in a simulated atmospheric boundary layer", J. Wind Eng. Ind. Aerodyn. Vol.73, pp. 45-58
19. S.J. Lee and C.W. Park, 1999, "Surface-pressure characteristics on a triangular prism located behind a porous fence", J. Wind Eng. Ind. Aerodyn., Vol. 80, pp. 69-83
20. S.J. Lee and C.W. Park, 2000, "The shelter effect of porous wind fences on coal piles in POSCO open storage yard", J. Wind Eng. & Industrial Aero., Vol.84, pp.101-118
21. M.D.A.E.S. Perera, 1981, "Shelter behind two-dimensional solid and porous fences", J. Wind Eng. Ind. Aerodyn. Vol.8, pp.93-104
22. J.K. Raine and D.C. Stevenson, 1977, "Wind protection by model fences in a simulated atmospheric boundary layer", J. Ind. Aerodyn. Vol.2, pp.159-180
23. D.S. Shin, J. Choi and S.J. Lee, 2000, "Velocity field measurement of flow inside snout of Zinc plating process using a single-frame PIV technique", ISIJ International, Vol.40, pp.484-490
24. C.E. Willert, and M. Gharib, 1991, "Digital particle image velocimetry," Exp. Fluids, Vol.10, pp.181-193
25. J. Westerweel, D. Dabiri and M. Gharib, 1997, "The effect of a discrete window offset on the accuracy of cross-correlation analysis of digital PIV recordings", Exp in Fluids, Vol.23, pp.20-28
26. J. Xuan and W. Ye, 1993, "Wind tunnel modeling of dust emission and deposition in lower atmosphere: similarity principles", Proc. 3rd Asia-Pacific Symp. on Wind Eng., pp.1053-1058
27. K.W. Yun, "Designing a function-enhanced suction accumulator for rotary compressor," pp.655~659